

Article

Computational Investigation of Nickel-Mediated B–H Activation and Regioselective Cage B–C(sp²) Coupling of *o*-Carborane

Wei-Hua Mu ^{1,*}, Wen-Zhu Liu ¹, Rui-Jiao Cheng ¹, Li-Juan Dou ¹, Pin Liu ¹ and Qiang Hao ^{2,*}

¹ Faculty of Chemistry and Chemical Engineering, Yunnan Normal University, Kunming 650092, China; lwz1464@163.com (W.-Z.L.); chrj2425@163.com (R.-J.C.); dlj1447@163.com (L.-J.D.); liupin6306@sina.com (P.L.)

² School of Chemistry and Chemical Engineering, Liaoning Normal University, Dalian 116029, China

* Correspondence: weihua_mu@ynnu.edu.cn (W.-H.M.); qh@lnnu.edu.cn (Q.H.)

Received: 30 April 2019; Accepted: 14 June 2019; Published: 18 June 2019



Abstract: Density functional theory (DFT) methods including LC- ω PBE, CAM-B3LYP, B3LYP, and B3LYP-D3, combined with double Zeta all-electron DZVP basis set, have been employed to conduct computational investigations on nickel-mediated reaction of *o*-carboranylzirconacycle, *n*-hexene, and 2-bromophenyltrimethylsilylacetylene in toluene solution. A multistep mechanism leading to the C,C,B-substituted carborane-fused tricyclics, including (1) sequential insertion of alkene and alkyne into Ni–C bonds; (2) double 1,2-migration of the TMS group; (3) B–H activation assisted by Cs₂CO₃ additive; and (4) reduction cage B–C (sp²) coupling, was proposed. Among these steps, the B–H activation of *o*-carborane was located as rate-determining step (RDS). With assistance of Cs₂CO₃ additive (replaced by K₂CO₃ in simulation), the RDS free-energy barrier at PCM-LC- ω PBE/DZVP level was calculated to be 23.1–23.9 kcal·mol^{−1}, transferring to a half-life of 3.9–15.1 h at 298 K. The predicted half-life coincides well with 80% experimental yields of C,C,B-substituted carborane-fused tricyclics after 12 h. Kinetic data obtained by employing LC- ω PBE method also reproduced the experimental diastereoselective ratio well. Various B–H activation pathways with and without Cs₂CO₃ additive were taken into consideration, which illustrates Cs₂CO₃ as an essential guarantee for smooth occurrence of this reaction at room temperature.

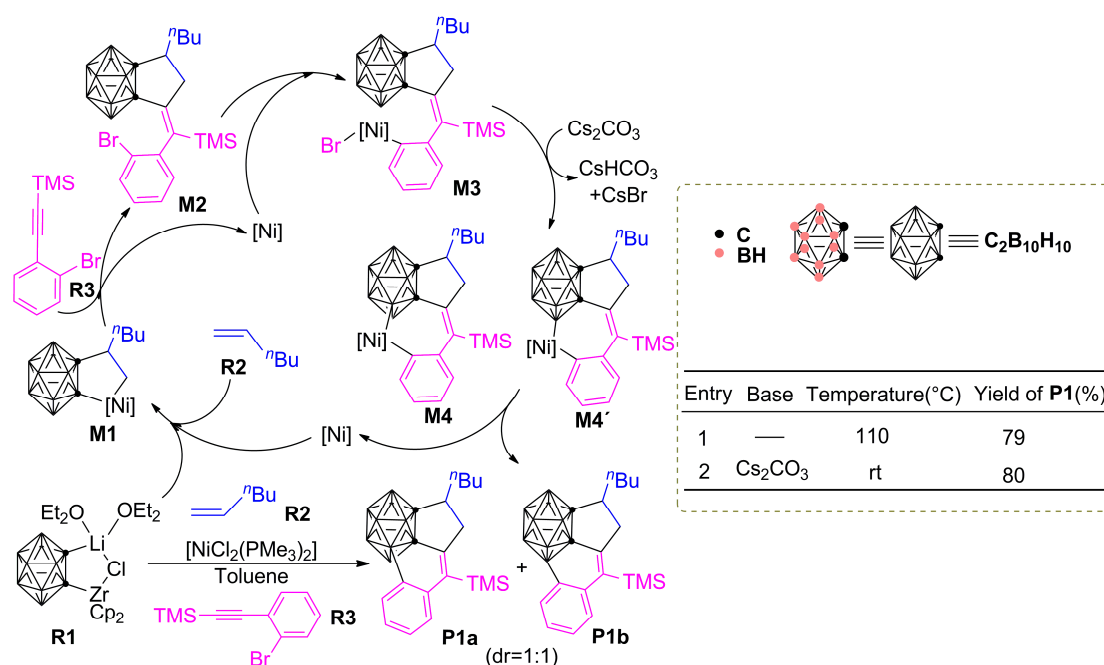
Keywords: *o*-carborane; B–H activation; nickel; diastereoselectivity; DFT

1. Introduction

Icosahedral *o*-carborane is a class of boron hydride clusters, in which two adjacent B–H vertices are replaced by C–H units, and has potential applications in boron neutron capture therapy (BNCT), organic synthetic, cancer treatment, drug development, and supramolecular design [1–7]. Due to its unique electronic properties and geometrical structure, the icosahedral *o*-carborane possesses unusual reactivity and can be activated by transition metal through C–H or B–H activation, to form a wide variety of *o*-carborane derivatives [8–13]. Remarkable achievements, in terms of substrate expansion, optimization of experimental conditions, and product yield enhancement, have been made in C–H activation and functionalization of *o*-carborane in recent years [8,9,14–16]. Based on computational simulations, some scholars have even presented reasonable explanations for reaction mechanisms and regioselectivity of C–H activation in *o*-carborane [17–23], which has also promoted the rapid development of this area.

However, owing to simultaneous existence of multiple B–H bonds with varying chemical environment, the regioselective activation of B–H bond in *o*-carborane remains a challenging topic

and has always been a focus in the field [10–13]. In recent decades, people have made significant achievements in nickel-catalyzed selective activation of B–H bonds in *o*-carborane, generally by introducing a directing group in substrates. For example, in 2010, Qiu and Xie had realized the palladium/nickel co-mediated [2+2+2] cyclization of 1-lithium-2-methyl-3-iodo-*o*-carborane with twice equivalent of alkynes, and prepared 1-C-3-B-substituted *o*-carborane derivative successfully [24]. This reaction has not only excellent yield but also good regioselectivity. In 2014, Xie's group had achieved three-component cyclization of *o*-carborane with olefin and halogenated phenyl alkyne through zirconium/nickel co-mediated coupling, and prepared a series of novel C,C,B-substituted carborane-fused tricyclics successfully (Scheme 1) [25]. This work represents the first example of cage B–C(sp²) coupling by direct B–H activation of *o*-carborane, which is of great significance for the regioselective B–H activation and functionalization of *o*-carborane derivatives. What particularly worth mentioning is, the reaction can process at room temperature and corresponding C,C,B-substituted carborane-fused tricyclics (**P1**) can be obtained with a yield up to 80% by adding Cs₂CO₃ additive (Entry 2 in Scheme 1).



Scheme 1. Nickel-mediated reaction of *o*-carboranylzirconacycle (**R1**), *n*-hexene (**R2**) and 2-bromophenyltrimethylsilylacetylene (**R3**).

Pioneered by previous reports [20,26], authors speculated that the reaction of *o*-carboranylzirconacycle (**R1**), *n*-hexene (**R2**) and 2-bromophenyltrimethylsilylacetylene (**R3**), as shown in Scheme 1, might go through the nickelacyclopentane intermediate **M1**, dihydrofulvenocarborane intermediates **M2** and **M3**, the nickelacycloheptene intermediates **M4** (or **M4'**) sequentially, and form the C,C,B-substituted *o*-carborane-fused tricyclic derivative **P1a/b** in the end. However, due to the limitation of experimental means in detecting unstable and reactive intermediates, the aforementioned mechanism is still under proposal. On the other hand, affected by many factors such as large size of *o*-carboranyl group, many electrons involved in transition metals, and diverse regioselectivities of *o*-carborane's B–H activation, it is really challenging in computational cost to conduct theoretical studies on transition metal catalyzed regioselective B–H activation of *o*-carborane. Our group has recently conducted a computational study on palladium-catalyzed regioselective B–H activation and arylation of *o*-carboranes with aryl iodides in solution, and found that the substituents on *o*-carborane have a significant effect on the regioselectivity of B–H activation [27]. In contrast to this, the presence of a fused five-membered ring in intermediates **M2** and **M3** (Scheme 1) here would

affect the regioselectivity of B–H activation significantly, and lead to different diastereoselectivities in the following cage B–C(sp²) coupling through direct B–H activation of *o*-carborane. Unfortunately, it is hard to confirm the validity of this speculation based on existing literature. Therefore, further theoretical research is required for better understanding of the reaction shown in Scheme 1.

To clarify the microscopic mechanism and rationalize experimentally detected diastereoselectivities of reaction shown in Scheme 1, density functional methods of LC- ω PBE, CAM-B3LYP, B3LYP, and B3LYP-D3, combining with the double- ζ all-electron DZVP basis set, were employed to conduct computational study on nickel-mediated B–H activation of *o*-carboranylzirconacycle with *n*-hexene and 2-bromophenyltrimethylsilylacetylene in toluene solution (Entry 2). For more accurate simulation, the experimentally operated reaction with none substituents truncated or simplified, was taken into consideration. The mechanism, diastereoselectivity of B–H activation, and role of Cs₂CO₃ additive will be explored and discussed in detail in the following parts.

2. Computational Details

All calculations reported here were performed with Gaussian 09 program [28], using an ultrafine integration grid of (99,590). LC- ω PBE [29,30], CAM-B3LYP [31], B3LYP [32,33] and B3LYP-D3 [34,35] density functional methods, as well as the double- ζ valence polarized (DZVP) [36,37] and triple- ζ valence polarized (TZVP) basis sets [38,39] employed in this paper were all set by default in Gaussian 09 program. All stationary points reported were confirmed by harmonic vibrational analyses based on geometrical optimizations employing DZVP basis set, in which all minima feature no imaginary frequency and all transition states feature only one imaginary frequency corresponding to correct reaction directions. To ensure that every transition state is connected to specific reactants, products or intermediates, intrinsic reaction coordinate (IRC) [40–42] track on key transition states were performed.

For better simulation of the reaction, experimentally performed toluene ($\epsilon = 2.37$) solvent effect were taken into consideration in both optimization and single-point calculation tasks, by employing a self-consistent reaction field (SCRF) polarization continuum model (PCM) [43,44] and isodensity-based SCRF radii (denoted IDSCRF) [45]. Unless noticed elsewhere, all Gibbs free energies reported in this article were obtained based on solution geometrical optimization in toluene, and corrected at experimental temperature (298 K) by using THERMO program [46]. During the revision of this manuscript, single-point calculations on stationary points at PCM-METHOD/TZVP//DZVP level (METHOD = LC- ω PBE, CAM-B3LYP, B3LYP, and B3LYP-D3 respectively) were performed wherever necessary. Considering both potassium and cesium elements belong to the same main group in periodic table and have similar electronic and chemical properties, we employed K₂CO₃ in place of Cs₂CO₃ in our simulations for convenience. Natural Bond Orbital (NBO) [47–49] analysis, as implemented in Gaussian 09 program, was also performed on selected stationary points to investigate their atomic charge population.

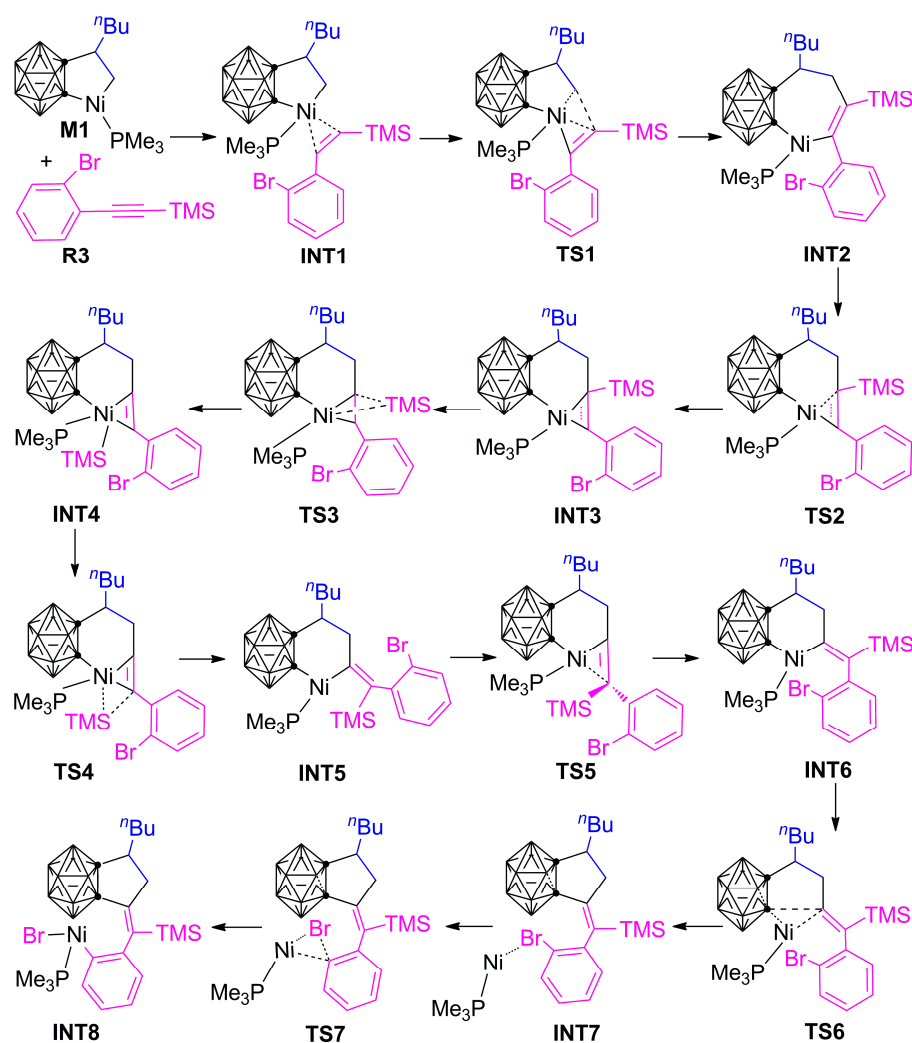
3. Results and Discussion

3.1. Mechanism

3.1.1. Formation Mechanism of Dihydrofulvenocarborane Intermediate INT8

We have firstly conducted calculations on the NiCl₂(PMe₃)₂-mediated reaction of *o*-carboranylzirconacycle (**R1**), *n*-hexene (**R2**) and 2-bromophenyltrimethylsilylacetylene (**R3**) at PCM-LC- ω PBE/DZVP level in toluene solution, with results presented in Scheme 2, Figures 1 and 2. According to previous reports [17], alkene insertion into the Ni–C bond is preferred over alkyne insertion when the Ni-carboranyl compound undergoes cycloaddition with alkene and alkyne. Also, in the presence of NiCl₂(PMe₃)₂, *o*-carboranylzirconacycle **R1** would interact with alkene **R2** and the catalyst to form a nickelacyclopentane intermediate **M1** by transmetalation [16,20,26], then **M1** complexes with alkyne to form a new compound **INT1** (Scheme 2). However, affected by variable

orientation of n Bu group in intermediate **M1** and subsequent B–H activation sites of *o*-carborane, the reaction shown in Scheme 1 led to a diastereoselective mixture of **P1a** and **P1b** (dr \approx 1:1) [25]. The later process of this reaction is totally different from the [2+2+1] cycloaddition of *o*-carborane with alkene and non-halogenated phenyl alkyne, in which none B–H activation occurred [26]. Based on PCM-LC- ω PBE/DZVP level's optimization in toluene solution, the formation of intermediate **M1** from **R1**, **R2** and the nickel catalyst is an exothermic process, releasing 26.0 kcal·mol⁻¹ of Gibbs free energies in total (See Figure S1 in the Supplementary File). For convenience, **M1**+**R3** is selected as the starting point of entire potential energy surfaces (PESs), and all discussion about reaction mechanism, diastereoselectivity, and the role of Cs₂CO₃ additive here were based on uniform orientation of n Bu group in **INT1**.



Scheme 2. Formation mechanism of the dihydrofulvenocarborane intermediate **INT8** from *o*-carborane compound **M1**+**R3**.

Owing to complexation between intermediate **M1** and alkyne **R3**, the bond lengths of Ni(3)–C(2), Ni(3)–C(4) and Ni(3)–P in **INT1** are calculated to be 1.93, 1.92 and 2.35 Å respectively, about 0.09, 0.06 and 0.08 Å lengthened when compared to their counterparts in **M1** (Figure 2). Meanwhile, the C(6)–C(7) bond in **INT1** is located at 1.24 Å, about 0.03 Å lengthened when compared to that in 2-bromophenyltrimethylsilylacetylene (**R3**). Both of this indicate that there is indeed some complexation interaction between 2-bromophenyltrimethylsilylacetylene (**R3**) and the nickel center in **INT1**. When C(6) atom in **INT1** gets nearer to C(4), alkyne **R3** would realize its insertion into the Ni–C bond through transition state **TS1**. As shown in Figure 1, the transformation from **INT1** to **INT2** through **TS1** needs

to get over a free-energy barrier of $5.9 \text{ kcal}\cdot\text{mol}^{-1}$ at PCM-LC- ω PBE/DZVP level. Considering **INT1**'s formation from **M1+R3** is exothermic of $4.7 \text{ kcal}\cdot\text{mol}^{-1}$ free energies, the transformation of **M1+R3** into **INT2** should be very fast at an experimental temperature of 298 K. In **TS1**, the bond length of C(4)–C(6) is located at 2.16 \AA . Due to the insertion of 2-bromophenyltrimethylsilylacetylene (**R3**), the bond length of Ni(3)–C(4) increased from 1.92 \AA (in **INT1**) to 1.96 \AA (in **TS1**), and C(6)–C(7) bond is lengthened to 1.29 \AA (Figure 2), showing a tendency to become a C=C double bond.

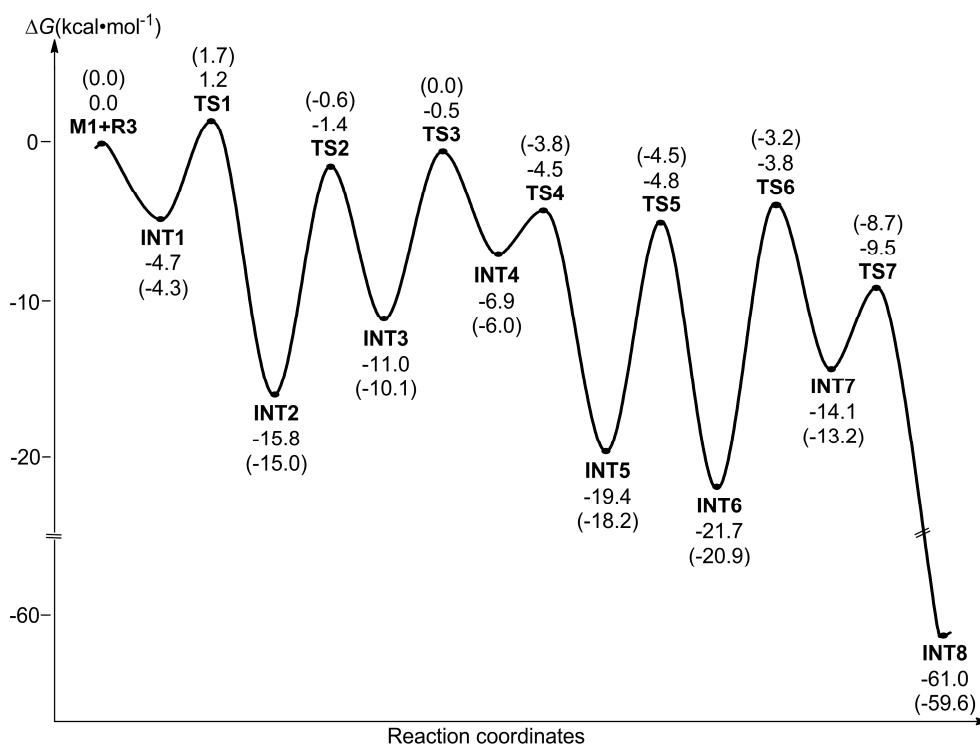


Figure 1. Relative Gibbs free energies (298 K, $\text{kcal}\cdot\text{mol}^{-1}$) for the formation of intermediate **INT8** from **M1+R3**, obtained at PCM-LC- ω PBE/DZVP level in toluene solution. The single-point calculation results obtained by employing TZVP basis set are presented in parentheses for comparison.

Intermediate **INT2** formed from **INT1** through transition state **TS1** is exothermic of $11.1 \text{ kcal}\cdot\text{mol}^{-1}$ in energy, and can isomerize to another intermediate **INT3** by getting over a free-energy barrier of $14.4 \text{ kcal}\cdot\text{mol}^{-1}$ (**TS2** in Figure 1). In **INT3**, the bond length of Ni–C(6) is shortened from 2.19 \AA (in **INT2**) to 1.94 \AA (Figure 2), indicating that intermediate **INT3** has the characteristics of an alkenyl nickel complex. Then, with assistance of the nickel center, TMS group in **INT3** will migrate from C(6) to C(7) through double 1,2-migration, as demonstrated in Scheme 2. The Gibbs free-energy barriers corresponding to the migration processes are 10.5 (**TS3**) and $2.4 \text{ kcal}\cdot\text{mol}^{-1}$ (**TS4**) respectively, which can be easily overcome at corresponding experimental temperature (298 K). Since intermediate **INT4** formed through the first 1,2-migration of TMS group is relatively unstable (Figure 1), it will be rapidly converted into a more stable nickelahexane intermediate **INT5**. In **INT5**, the bond lengths of Ni–C(2) and Ni–C(6) are 1.89 and 1.76 \AA , respectively (Figure 2), indicates effective coordination between Ni atom and C(2)/C(6) atoms.

Thereafter, to promote the B–H activation and subsequent cage B–C(sp^2) coupling of *o*-carborane, as well as effectively reduce the steric hindrance between TMS and PMe_3 groups, intermediate **INT5** will convert to intermediate **INT6** through transition state **TS5**. The Gibbs free-energy barrier corresponding to **TS5** is $14.6 \text{ kcal}\cdot\text{mol}^{-1}$, about 0.2 and $4.1 \text{ kcal}\cdot\text{mol}^{-1}$ higher than **TS2** and **TS3**, respectively (Figure 1). It is deemed that the stabilization from the catalytic center has played an essential role in facilitating this dihedral flip process [20] and ensured its easy occurrence at room temperature. After the formation of intermediate **INT6**, it would undergo reduction elimination via

transition state **TS6** and convert itself to a carboranyl-cyclopentane derivative **INT7**, which requires to get across a free-energy barrier of $17.9 \text{ kcal}\cdot\text{mol}^{-1}$. Although the free-energy barrier corresponding to **TS6** is $3.3 \text{ kcal}\cdot\text{mol}^{-1}$ higher than **TS5** (Figure 1), it can still be easily overcome at an experimental temperature of 298 K.

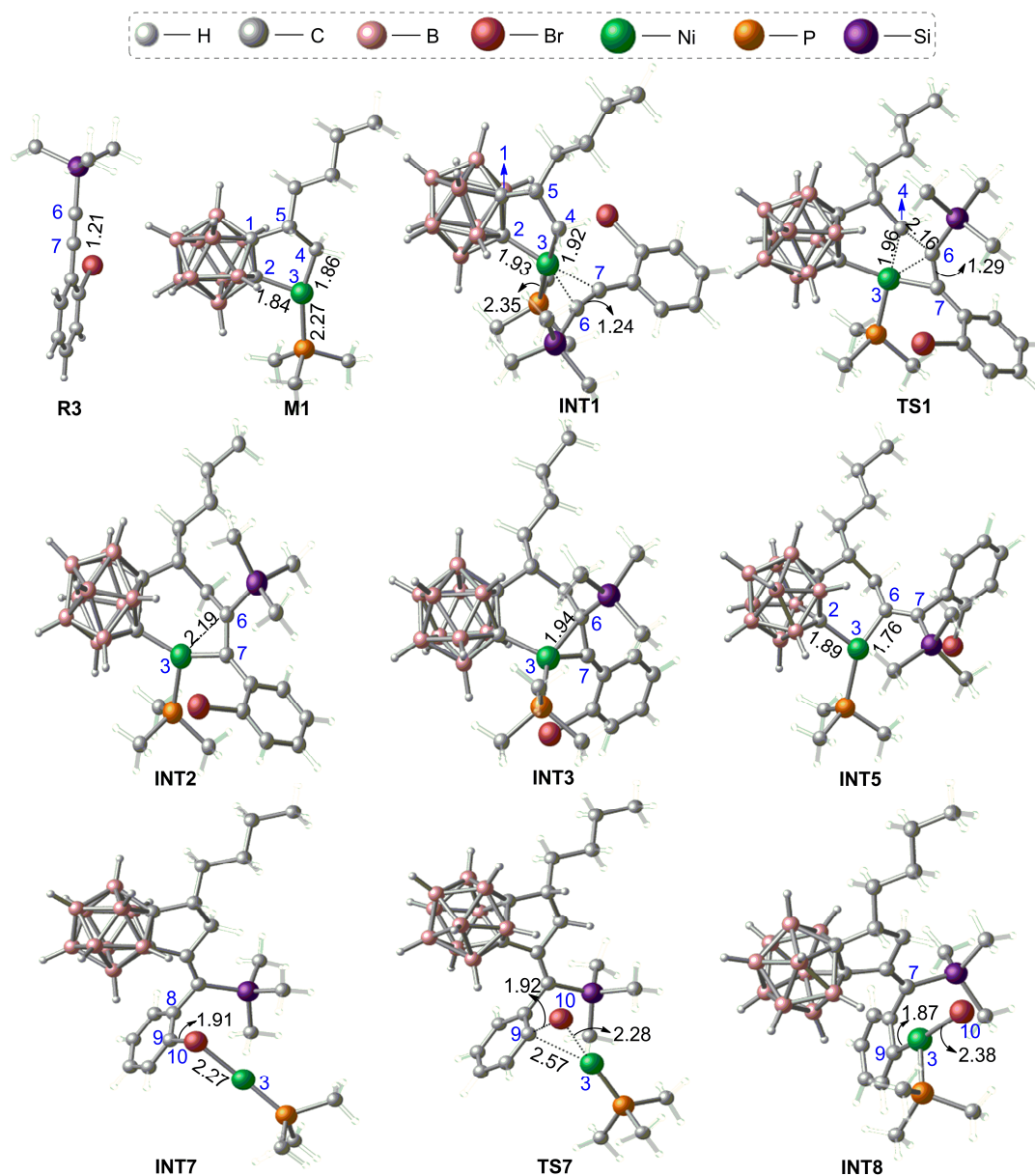


Figure 2. Optimized structures and key geometrical parameters (bond length in Å) for stationary points involved in the formation of intermediate **INT8** from **M1**+**R3**. For clarity, all noncritical atoms especially hydrogens were made transparent, and all structures not referred directly in the text were presented in Figure S2.

As shown in Figure 1 and Scheme 2, the nickel center (NiPMe_3) in complex **INT7** can easily realize its insertion into the phenyl $\text{C}(\text{sp}^2)\text{-Br}$ bond through transition state **TS7**, and convert itself to a more stable intermediate **INT8** meanwhile. Successful location of **INT8** verifies the rationality of experimentally proposed existence of intermediate **M3** in Scheme 1. This process only needs to overcome a free-energy barrier of $4.6 \text{ kcal}\cdot\text{mol}^{-1}$. On contrary, the leaving of NiPMe_3 fragment needs to absorb $20.4 \text{ kcal}\cdot\text{mol}^{-1}$ free energies (Figure S3), which indicates the speculated intermediate **M2** in Scheme 1 seems not on the optimal pathway. In transition state **TS7**, the bond length of $\text{C}(9)\text{-Br}$ is

extended from 1.91 Å (in **INT7**) to 1.92 Å, showing small tendency of stretch and breaking (Figure 2). The bond lengths of C(9)–Ni and Br–Ni bonds in intermediate **INT8** are calculated to be 1.87 and 2.38 Å respectively, indicates that the nickel center has inserted into the C(9)–Br bond completely. The formation of intermediate **INT8** lays an essential foundation for subsequent B–H activation and final generation of the C,C,B-substituted *o*-carborane-fused tricyclic product **P1a/b**.

Hoping for more accurate energy results, we have further conducted single-point calculation by employing a larger TZVP basis set based on the DZVP optimized geometries. As what presented in parentheses in Figure 1, only tiny deviation of TZVP free-energy results from DZVP ones can be observed, similar to what found out by Řezáč and co-authors [50].

3.1.2. Mechanism of B–H Activation and Cage B–C(sp²) Coupling of *o*-Carborane

To investigate the B–H activation and cage B–C (sp²) coupling mechanism of *o*-carborane, we then conducted calculations on the B(11)–H activation of intermediate **INT8** at PCM-LC- ω PBE/DZVP level in toluene solution, with corresponding results summarized in Figures 3 and 4. The diastereoselective formation of **P1b** through B(17)–H activation will be discussed in part 3.3 in the following.

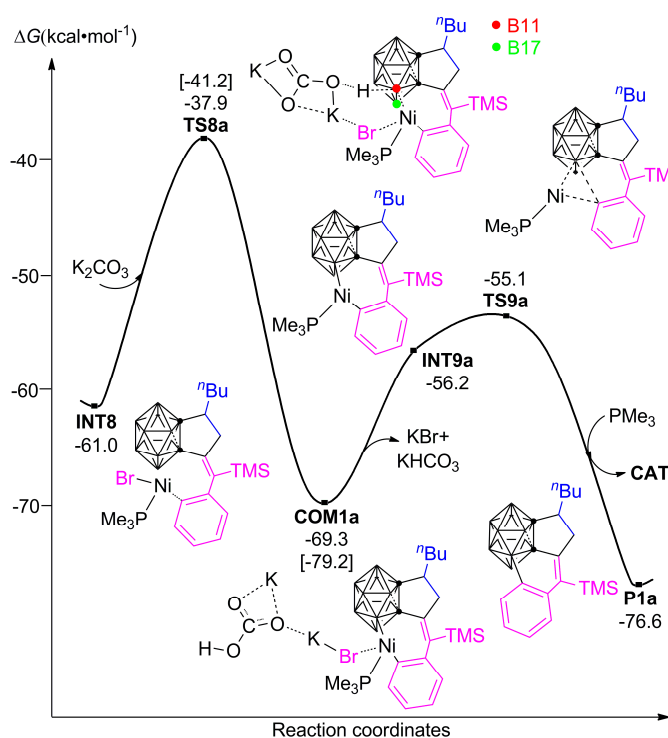


Figure 3. Most probable mechanism and relative Gibbs free energies (298 K, kcal·mol^{−1}) for B(11)–H activation and cage B–C(sp²) coupling of intermediate **INT8**, obtained at PCM-LC- ω PBE/DZVP level in toluene solution. Free-energy results obtained by employing Cs₂CO₃ are presented in square brackets for comparison.

As shown in Figure 3, when Cs₂CO₃ (replaced by K₂CO₃ firstly, See Figure S4 and line 373–386 for details) is available in the reaction, intermediate **INT8** will be converted to complex **COM1a** through activation of the spatially most favorable B(11)–H (**TS8a**). The free-energy barrier corresponding to **TS8a** is calculated to be 23.1 kcal·mol^{−1} at PCM-LC- ω PBE/DZVP level, which is 5.2 kcal·mol^{−1} higher than that of **TS6** (17.9 kcal·mol^{−1}, represents the highest barrier before **TS8a**). The reaction rate constant converted from free-energy barrier of **TS8a** is 7.113 × 10^{−5} L·mol^{−1}·s^{−1}, which is significantly smaller than any of that transferred from free-energy barriers of **TS1–TS7** (Table S1). Taking the whole PESs (Figures 1 and 3) into consideration, the B(11)–H activation process of intermediate **INT8** (via **TS8a**)

features the highest barrier ($23.1 \text{ kcal}\cdot\text{mol}^{-1}$), which indicates significant limit of **TS8a** on the overall reaction rate, and is therefore the rate-determining step (RDS) of entire reaction.

In transition state **TS8a**, the activation of B(11)–H and synchronous formation of Ni–B(11) bond is realized under the help of K_2CO_3 additive, through an interaction between one oxygen atom in CO_3^{2-} ion and the migrated H(12) atom (Figure 4). The bond lengths of B(11)–H(12), H(12)–O(13), Ni–B(11) and Ni–Br bonds in **TS8a** are calculated to be 1.46, 1.40, 2.09 and 2.46 Å respectively, in accordance with subsequent formation of KHCO_3 and KBr fragments. As depicted in Figure 3, complex **COM1a** would drop KHCO_3 and KBr fragments and transform itself into intermediate **INT9a**, being endothermic of $13.1 \text{ kcal}\cdot\text{mol}^{-1}$ of free energies.

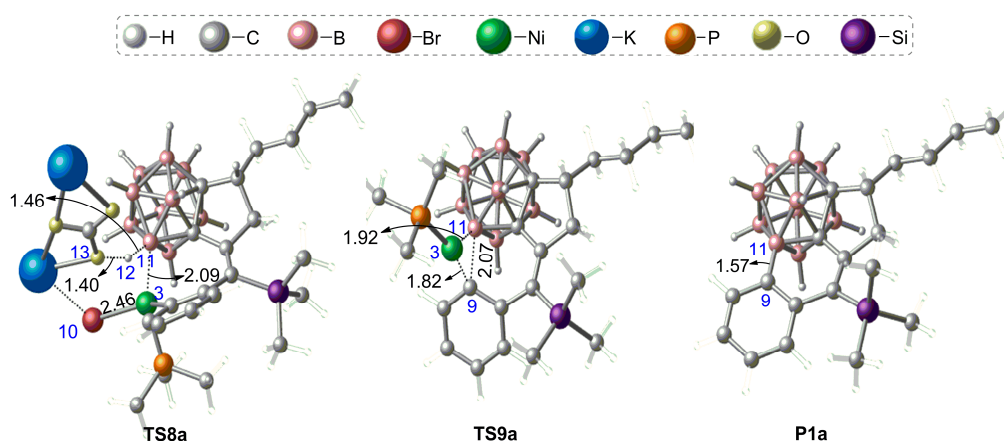


Figure 4. Optimized structures and key geometrical parameters (bond length in Å) for stationary points involved in the B(11)–H activation and cage B–C(sp^2) coupling process of intermediate **INT8**. For clarity, all noncritical atoms especially hydrogens were made transparent, and all structures not referred directly in the text were presented in Figure S2.

Finally, the direct cage B–C(sp^2) coupling in intermediate **INT9a** is achieved through coupling of B(11) and C(9) in transition state **TS9a**, and the C,C,B-substituted carborane-fused product **P1a** is formed through reduction elimination, accompanied by regeneration of the $\text{Ni}(\text{PMe}_3)_2$ catalyst (**CAT**). As shown in Figure 3, the conversion of **COM1a** to **P1a** via **INT9a** and **TS9a** requires overcoming a free-energy barrier of $14.2 \text{ kcal}\cdot\text{mol}^{-1}$ (**TS9a**) in total, which should be smooth under experimental temperature of 298 K. The bond length of C(9)–B(11) in the final product **P1a** is shortened from 2.07 Å (in **TS9a**) to 1.57 Å, suggests B(11) on *o*-carboranyl group has successfully coupled with C(9) on the phenyl group (Figure 4).

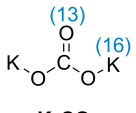
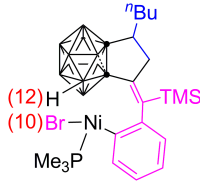
3.2. The Role of Cs_2CO_3 Additive

As a commonly used basic additive, Cs_2CO_3 is widely used in various reactions [51–55]. To investigate detailed interaction mechanism of Cs_2CO_3 with intermediate **INT8** in this reaction, we have explored another two paths (**Path a1** and **a2**, Figure 5) at the same computational level.

In the absence of Cs_2CO_3 additive (replaced by K_2CO_3 in simulation, **Path a1**), the B(11)–H bond on *o*-carboranyl group in intermediate **INT8** can only be activated under the help of –Br group. As shown in Figure 5, the C,C,B-substituted carborane-fused tricyclic product **P1a** is formed concurrently with removal of one HBr molecule and regeneration of **CAT**. The free-energy barrier corresponding to **TS8a1** on **Path a1** is calculated to be $36.9 \text{ kcal}\cdot\text{mol}^{-1}$, about $13.8 \text{ kcal}\cdot\text{mol}^{-1}$ higher than that of **TS8a** on **Path a**. These results indicate that the Cs_2CO_3 additive does play an essential role in the activation of B(11)–H bond of **INT8**, and explains why the reaction needs to be carried out at a higher temperature (383 K) in the absence of Cs_2CO_3 additive (Entry 1 in Scheme 1). For the case in which K_2CO_3 is present but only help to stabilize the leaving HBr fragment through its positive charge center (K atom, **Path a2** in Figure 5), the free-energy barrier corresponding to transition state **TS8a2** is still as high as

charge distributed prefers migrating to O(13) atom. Eventually, the KHCO_3 and KBr fragments are formed and drop. These NBO charge population results reproduce aforementioned energetic results well, and confirms **Path a**'s dominance in generating C,C,B-substituted carborane-fused tricyclics **P1a**.

Table 1. NBO charge population of key atoms in intermediate **INT8** and K_2CO_3 additive, obtained at PCM-LC- ω PBE/DZVP//DZVP level in toluene solution (unit: \bar{e}).

	NBO charge	
 K_2CO_3	Br(10)	-0.480
	H(12)	+0.041
 INT8	O(13)	-1.055
	K(16)	+0.932

3.3. Diastereoselectivity of B–H Activation of *o*-Carborane

Many experiments show diverse site-selectivities of B–H activation in different *o*-carborane-involved reactions [13,25,57], but few of these had been rationalized by computational explorations. According to Quan's experiments [25], only B(11)–H and B(17)–H (Figure 6) could be activated and corresponding **P1a/b** ($\text{dr} \approx 1:1$) products can be detected experimentally (Scheme 1), while B(19)–H or B(20)–H activation products can be obtained in other similar *o*-carborane-involved reactions [57]. The authors speculated that the specific diastereoselectivity in this reaction was due to coexistence of *o*-carborane cage and the fused five-membered ring in intermediate **INT8**, which hindered free rotation of the phenyl group [25].

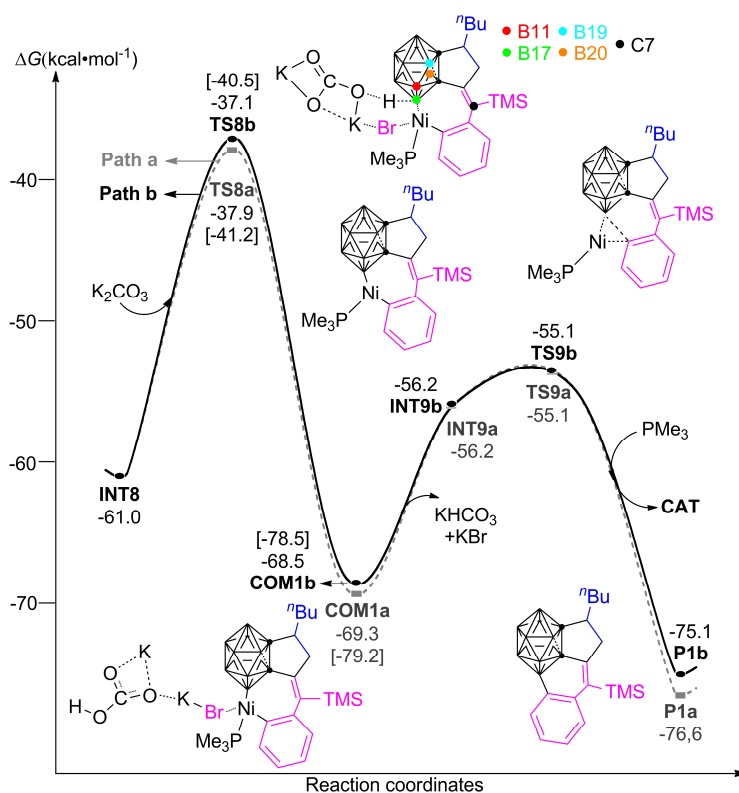


Figure 6. Probable mechanism and relative Gibbs free energies (298 K, $\text{kcal}\cdot\text{mol}^{-1}$) for B(17)–H activation and cage B–C(sp^2) coupling of intermediate **INT8**, obtained at PCM-LC- ω PBE/DZVP level in toluene solution. **Path a** is plotted in grey dotted line for comparison. Free-energy results obtained by employing Cs_2CO_3 are presented in square brackets for comparison.

Based on computational optimization and careful check for the geometry of intermediate **INT8**, we found the presence of the fused five-membered ring in **INT8** greatly limits the reachable range of groups on C(7) atom (Figures 2 and 6), and thus keeps -Br group on the phenyl ring far away from B(19)-H and B(20)-H on *o*-carboranyl group. In other words, the rigidity of *o*-carborane cage and the fused five-membered ring in **INT8** greatly hinders -Br group on the phenyl ring from getting near to other B-Hs (such as B(19)-H and B(20)-H) except for B(11)-H and B(17)-H on *o*-carboranyl group. Therefore, B(19)-H and B(20)-H could not be activated, only C,C,B-substituted products **P1a/b** (dr \approx 1:1) generated through B(11)/B(17)-H activation can be detected in corresponding experiments.

To investigate the diastereoselectivity of B-H activation in this reaction, calculations at PCM-LC- ω PBE/DZVP level were performed on **Path b**, with corresponding energy and geometrical results presented in Figure 6 and Figure S6, respectively. Similar to **Path a**, transition state **TS8b** on **Path b**, which corresponds to B(17)-H activation in **INT8**, is also located as the RDS of entire reaction. The free-energy barrier corresponding to **TS8b** is calculated to be 23.9 kcal·mol⁻¹. A 0.8 kcal·mol⁻¹ higher free-energy barrier of **TS8b** than **TS8a** converts to a diastereoselective ratio (dr, **P1a:P1b**) of about 3.9:1 (Table 2), coincides well with corresponding experimental dr value (\sim 1:1).

Aiming at better prediction of experimental diastereoselectivities, we employed three different methods (CAM-B3LYP, B3LYP, and B3LYP-D3) and recomputed the optimal **Path a** and **b** (as shown in Figures 3 and 6). All stationary points on the PESs were re-optimized and characterized under the same condition but using different density functionals. The free-energy results and corresponding kinetic parameters obtained at PCM-LC- ω PBE/DZVP (denoted LC- ω PBE), PCM-CAM-B3LYP/DZVP (denoted CAM-B3LYP), PCM-B3LYP/DZVP (denoted B3LYP) and PCM-B3LYP-D3/DZVP (denoted B3LYP-D3) levels were summarized in Table 2, with complete potential energy profiles presented in Figure S7 and relative Gibbs free energies summarized in Table S2.

Table 2. Free-energy barriers (in kcal·mol⁻¹) and corresponding kinetic data for RDSs (**TS8a/b** or **TS9a/b**).

Methods	LC- ω PBE	CAM-B3LYP	B3LYP	B3LYP-D3	
Free-energy barriers ($\Delta\Delta G_r$, kcal·mol ⁻¹)	TS8a	23.1	24.8	26.7	15.2
	TS8b	23.9	26.9	29.6	14.3
	TS9a	14.2	10.3	3.1	22.1
	TS9b	13.4	8.9	6.9	23.1
$k_{RDS,a}$ (L·mol ⁻¹ ·s ⁻¹)	7.113×10^{-5}	4.030×10^{-6}	1.629×10^{-7}	3.850×10^{-4}	
$k_{RDS,b}$ (L·mol ⁻¹ ·s ⁻¹)	1.842×10^{-5}	1.162×10^{-7}	1.216×10^{-9}	7.113×10^{-5}	
$t_{1/2,RDS,a}$ (h)	3.905×10^0	6.893×10^1	1.705×10^3	5.002×10^{-1}	
$t_{1/2,RDS,b}$ (h)	1.508×10^1	2.390×10^3	2.283×10^5	2.707×10^0	
dr ^{Calc.}	3.9:1	35:1	134:1	5.4:1	
dr ^{Expt.}	1:1				

As shown in Table 2, the RDS predicted by B3LYP and CAM-B3LYP methods are the same as what predicted by LC- ω PBE method, which correspond to the activation of B(11)-H through **TS8a** or activation of B(17)-H through **TS8b** respectively. Gibbs free-energy barriers of the RDS (**TS8a/b**) predicted by LC- ω PBE, CAM-B3LYP, and B3LYP methods are calculated to be 23.1/23.9, 24.8/26.9 and 26.7/29.6 kcal·mol⁻¹ respectively; however, when D3 dispersion option was taken into consideration in B3LYP method (denoted B3LYP-D3), the free-energy barriers of **TS8a/b** are significantly reduced and get much lower than those predicted by LC- ω PBE, CAM-B3LYP and B3LYP methods (14.3–15.2 vs. 23.1–29.6 kcal·mol⁻¹, Table 2). The dramatic decrease of **TS8a/b**'s barriers, probably arisen from overweight of the weak interaction [58,59] between KHCO₃, KBr and other fragments in **TS8a/b**, makes the next reduction elimination step (**INT9a/b** \rightarrow **TS9a/b** \rightarrow **P1a/b**) become RDS of the whole reaction.

The reaction rate constants and half-lives predicted by CAM-B3LYP and B3LYP methods show 1–5 orders of magnitude deviation from corresponding experimental time and yield (80% after 12 hours,

Scheme 1). Taking the gold standard of current computational methods (1.0 kcal·mol⁻¹) [60] into consideration, these free-energy barriers obtained by employing CAM-B3LYP and B3LYP methods are reasonable but relatively higher. Satisfactorily, the reaction rate constants and half-lives predicted by LC- ω PBE and B3LYP-D3 methods show only 0–1 orders of magnitude deviation from experimental data, more accurate and reasonable when compared to experimental results. Considering B3LYP-D3 method may have overestimated the dispersion contribution [58,59] and reflected the free-energy barrier of B–H activation (**TS8a/b**) inaccurately, the RDS free-energy barriers, reaction rate constants and half-lives derived from LC- ω PBE method are closest to corresponding experimental data. Additionally, the diastereoselective ratio (dr) of **P1a** to **P1b** predicted by LC- ω PBE method is about 3.9:1, also coincides best with corresponding experimental results (Table 2).

For further confirmation of **TS8a/b** (or **TS9a/b** for B3LYP-D3 method)'s RDS character, full optimizations about stationary points lying on the PESs from **M1+R3** to **INT8** were performed at PCM-CAM-B3LYP/DZVP, PCM-B3LYP/DZVP and PCM-B3LYP-D3/DZVP levels. Corresponding Gibbs free-energy barriers of transition states **TS1–TS7** are summarized in Table 3, with detailed potential energy profiles shown in Figure S8 and relative Gibbs free energies summarized in Table S3. Except for the free-energy barrier of **TS6** employing B3LYP-D3 method is of equivalence to that of **TS9a/b** (22.4 vs. 22.1–23.1 kcal·mol⁻¹), all other free-energy barriers of transition states **TS1–TS7** are much lower than **TS8a/b**. These results obtained by employing LC- ω PBE, CAM-B3LYP and B3LYP methods illustrate that **TS8a/b** is indeed the RDS, and the B–H activation process has a decisive influence on the overall rate of this reaction. Further single-point calculations employing CAM-B3LYP, B3LYP, and B3LYP-D3 methods, combined with a larger TZVP basis set also show very small deviation in energy from the DZVP optimized ones (Figure S8), indicating the rationality of employing DZVP basis set in current simulation again.

Table 3. Free-energy barriers ($\Delta\Delta G$, kcal·mol⁻¹) for transition states **TS1–TS7**, obtained at PCM- LC- ω PBE/DZVP (denoted LC- ω PBE), PCM-CAM-B3LYP/DZVP (denoted CAM-B3LYP), PCM-B3LYP/DZVP (denoted B3LYP) and PCM-B3LYP-D3/DZVP (denoted B3LYP-D3) levels in toluene solution at 298 K.

Transition States	Free-energy Barriers ($\Delta\Delta G$, kcal·mol ⁻¹)			
	LC- ω PBE	CAM-B3LYP	B3LYP	B3LYP-D3
TS1	5.9	12.2	19.1	10.8
TS2	14.4	16.0	14.3	12.9
TS3	10.5	14.9	15.6	15.2
TS4	2.4	1.0	1.6	2.1
TS5	14.6	18.8	19.3	17.7
TS6	17.9	23.9	22.3	22.4
TS7	4.6	5.4	4.7	2.1

Finally, to investigate the rationality of replacing Cs₂CO₃ with K₂CO₃ in our simulation, **Path a** and **b** employing Cs₂CO₃ have been tested at PCM-LC- ω PBE/DZVP (SDD [61] for Cs) level (Entry 2 in Figure S4), with corresponding energetic results presented in square brackets in Figures 3 and 6 respectively. Although non-negligible energy differences for stationary points can be observed when K₂CO₃ is employed in place of Cs₂CO₃, the mechanism trends in these two cases coincide well with each other. Results based on PCM-LC- ω PBE/DZVP optimization employing both Cs₂CO₃ and K₂CO₃ can predict rational dr ratio of **P1a:P1b** (3.3:1 and 3.9:1 respectively, Entry 1–2); however, the half-lives derived from RDS barriers employing Cs₂CO₃ additive deviate two orders of magnitude from corresponding experimental time (12 h). Further optimization at PCM-LC- ω PBE/TZVP (SDD for Cs) level (Entry 3–4) give out similar mechanistic and energetic results with the DZVP ones, indicating no necessity for full optimization employing TZVP basis set in current simulation. Taking both the predicted half-life and dr value into account, the PCM-LC- ω PBE/DZVP level's results by employing K₂CO₃ additive coincide best with corresponding experimental time and yield (80% after 12 h).

4. Conclusions

In summary, density functional theory (DFT) at PCM-LC- ω PBE/DZVP, PCM-CAM-B3LYP/DZVP, PCM-B3LYP/DZVP, and PCM-B3LYP-D3/DZVP levels have been employed to conduct computational investigations on Ni(PMe₃)₂-mediated reaction of *o*-carboranylzirconacycle (**R1**), *n*-hexene (**R2**) and 2-bromophenyltrimethylsilylacetylene (**R3**) in toluene solution. The following conclusions can be drawn: (1) This reaction is a multistep process, in which more than an intermediate such as nickelacyclopentane, nickelacycloheptene, nickelacyclohexane, and dihydrofulvenocarborane intermediates are involved. With the assistance of Cs₂CO₃ additive, the rate-determining B–H activation of dihydrofulvenocarborane intermediate **INT8** are smoothly achieved at room temperature. Finally, the *o*-carboranyl cage B–C(sp²) phenyl coupling and corresponding C,C,B-substituted *o*-carborane-fused tricyclics (**P1a/b**) are obtained through reduction elimination, accompanying by regeneration of the Ni(PMe₃)₂ catalyst. (2) The Cs₂CO₃ additive is directly involved in *o*-carborane's B–H activation, and it can dramatically reduce the RDS's free-energy barriers through stabilizing corresponding transition structures (**TS8a/b**). It is deemed that the addition of Cs₂CO₃ ensures this reaction's smooth proceeding at room temperature. (3) Computational results obtained by employing LC- ω PBE, CAM-B3LYP, and B3LYP functionals indicate the activation of B(11)–H or B(17)–H bonds in dihydrofulvenocarborane intermediate **INT8** is the RDS of the entire reaction. The Gibbs free-energy barriers for RDS (**TS8a/b**) at PCM-LC- ω PBE/DZVP level is calculated to be 23.1–23.9 kcal·mol^{−1}, transferring to half-lives of 3.9–15.1 h. The predicted half-lives exhibit small deviation from experimental yield and time (80% in 12 h). The diastereoselective ratio (dr) of **P1a** to **P1b** predicted by LC- ω PBE method is about 3.9:1, also reproduces corresponding experimental observation (**P1a:P1b** \approx 1:1) well.

Supplementary Materials: The following are available online at <http://www.mdpi.com/2073-4344/9/6/548/s1>, Figure S1: **M1**'s formation from **R1**+**CAT1**+**R2**, Figures S2 and S6: Optimized structures and key geometrical parameters for stationary points, Figure S3: Relative Gibbs free energies of **M2**, Figure S4: PESs employing Cs₂CO₃ and K₂CO₃, Figure S5: Part PESs for **Path a3** and **a4**, Figure S7: PESs for B(11)/B(17)–H activation in **INT8**, obtained at different computational levels, Figure S8: PESs for intermediate **INT8**'s formation from **M1**+**R3**, obtained at different computational levels, Table S1: Free-energy barriers and corresponding kinetic data for transition states **TS1**–**TS7** and **TS8a**, Tables S2–S3: Relative Gibbs free energies for stationary points on **Path a** and **b**, obtained at different computational levels, Tables S4, S7 and S13: Optimized Cartesian coordinates for stationary points, Tables S5, S8 and S14: Vibrational frequencies for stationary points, Tables S6, S9–S12 and S15–S17: Energetic results for stationary points, obtained at different computational levels.

Author Contributions: Data curation, W.-H.M., W.-Z.L., Q.H. and R.-J.C.; Funding acquisition, W.-H.M.; Project administration, W.-H.M.; Visualization, W.-Z.L.; Writing-original draft, W.-H.M. and W.-Z.L.; Writing-review and editing, W.-H.M., L.-J.D., P.L. and Q.H.

Acknowledgments: The authors acknowledge financial supports from the National Natural Science Foundation of China (grant number 21763033 and 21363028), as well as software supports from De-Cai Fang in College of Chemistry, Beijing Normal University.

Conflicts of Interest: The authors declare no conflict of interest.

References

1. Chen, G.; Yang, J.; Lu, G.; Liu, P.C.; Chen, Q.; Xie, Z.; Wu, C. One Stone Kills Three Birds: Novel Boron-Containing Vesicles for Potential BNCT, Controlled Drug Release, and Diagnostic Imaging. *Mol. Pharm.* **2014**, *11*, 3291–3299. [[CrossRef](#)] [[PubMed](#)]
2. Guo, J.; Liu, D.; Zhang, J.; Zhang, J.; Miao, Q.; Xie, Z. *o*-Carborane Functionalized Pentacenes: Synthesis, Molecular Packing and Ambipolar Organic Thin-film Transistors. *Chem. Commun.* **2015**, *51*, 12004–12007. [[CrossRef](#)] [[PubMed](#)]
3. Jin, G.F.; Hwang, J.-H.; Lee, J.-D.; Wee, K.-R.; Suh, I.-H.; Kang, S.O. A Three-Dimensional π -Electron Acceptor, Tri-Phenyl-*o*-Carborane, Bearing a Rigid Conformation with End-On Phenyl Units. *Chem. Commun.* **2013**, *49*, 9398–9400. [[CrossRef](#)] [[PubMed](#)]
4. Cioran, A.M.; Musteti, A.D.; Teixidor, F.; Krpetic, Ž.; Prior, I.A.; He, Q.; Kiely, C.J.; Brust, M.; Viñas, C. Mercaptocarborane-Capped Gold Nanoparticles: Electron Pools and Ion Traps with Switchable Hydrophilicity. *J. Am. Chem. Soc.* **2012**, *134*, 212–221. [[CrossRef](#)] [[PubMed](#)]

5. Scholz, M.; Hey-Hawkins, E. Carboranes as Pharmacophores: Properties, Synthesis, and Application Strategies. *Chem. Rev.* **2011**, *111*, 7035–7062. [[CrossRef](#)] [[PubMed](#)]
6. Jude, H.; Disteldorf, H.; Fischer, S.; Wedge, T.; Hawkrigde, A.M.; Arif, A.M.; Hawthorne, M.F.; Muddiman, D.C.; Stang, P.J. Coordination-Driven Self-Assemblies with a Carborane Backbone. *J. Am. Chem. Soc.* **2005**, *127*, 12131–12139. [[CrossRef](#)]
7. Grimes, R.N. Carboranes in the Chemist's Toolbox. *Dalton Trans.* **2015**, *44*, 5939–5956. [[CrossRef](#)]
8. Qiu, Z.; Xie, Z. Generation and Reactivity of *o*-Carborynes. *Dalton Trans.* **2014**, *43*, 4925–4934. [[CrossRef](#)]
9. Tang, C.; Xie, Z. Nickel-Catalyzed Cross-Coupling Reactions of *o*-Carboranyl with Aryl Iodides: Facile Synthesis of 1-Aryl-*o*-Carboranes and 1,2-Diaryl-*o*-Carboranes. *Angew. Chem. Int. Ed.* **2015**, *54*, 7662–7665. [[CrossRef](#)]
10. Lyu, H.; Quan, Y.; Xie, Z. Palladium-Catalyzed Direct Dialkenylation of Cage B-H Bonds in *o*-Carboranes Through Cross-Coupling Reactions. *Angew. Chem. Int. Ed.* **2015**, *54*, 10623–10626. [[CrossRef](#)]
11. Lyu, H.; Quan, Y.; Xie, Z. Transition Metal Catalyzed Direct Amination of the Cage B(4)-H Bond in *o*-Carboranes: Synthesis of Tertiary, Secondary, and Primary *o*-Carboranyl Amines. *J. Am. Chem. Soc.* **2016**, *138*, 12727–12730. [[CrossRef](#)] [[PubMed](#)]
12. Lyu, H.; Quan, Y.; Xie, Z. Rhodium-Catalyzed Regioselective Hydroxylation of Cage B-H Bonds of *o*-Carboranes with O₂ or Air. *Angew. Chem. Int. Ed.* **2016**, *55*, 11840–11844. [[CrossRef](#)] [[PubMed](#)]
13. Quan, Y.; Xie, Z. Palladium-Catalyzed Regioselective Diarylation of *o*-Carboranes by Direct Cage B-H Activation. *Angew. Chem. Int. Ed.* **2016**, *55*, 1295–1298. [[CrossRef](#)] [[PubMed](#)]
14. Zhao, D.; Xie, Z. Recent Advances in the Chemistry of Carborynes. *Coord. Chem. Rev.* **2016**, *314*, 14–33. [[CrossRef](#)]
15. Ren, S.; Qiu, Z.; Xie, Z. Transition-Metal-Promoted or -Catalyzed Exocyclic Alkyne Insertion via Zirconacyclopentene with Carborane Auxiliary: Formation of Symmetric or Unsymmetric Benzocarboranes. *J. Am. Chem. Soc.* **2012**, *134*, 3242–3254. [[CrossRef](#)] [[PubMed](#)]
16. Ren, S.; Qiu, Z.; Xie, Z. Three-Component [2+2+2] Cycloaddition of Carboryne, Unactivated Alkene, and Alkyne via Zirconacyclopentane Mediated by Nickel: One-Pot Synthesis of Dihydrobenzocarboranes. *Angew. Chem. Int. Ed.* **2012**, *51*, 1010–1013. [[CrossRef](#)] [[PubMed](#)]
17. Mu, W.-H.; Cheng, R.-J.; Fang, D.-C.; Chass, G.A. The Pivotal Role of Electronics in Preferred Alkene over Alkyne Ni-Carboryne Insertions and Absolute Regioselectivities. *Dalton Trans.* **2018**, *47*, 6494–6498. [[CrossRef](#)]
18. Zhao, D.; Zhang, J.; Xie, Z. An Unprecedented Formal [5+2] Cycloaddition of Nitrones with *o*-Carboryne via Tandem [3+2] Cycloaddition/Oxygen Migration/Aromatization Sequence. *J. Am. Chem. Soc.* **2015**, *137*, 13938–13942. [[CrossRef](#)]
19. Mu, W.-H.; Xia, S.-Y.; Li, J.-X.; Fang, D.-C.; Wei, G.; Chass, G.A. Competing Mechanisms, Substituent Effects, and Regioselectivities of Nickel-Catalyzed [2+2+2] Cycloaddition between Carboryne and Alkynes: A DFT Study. *J. Org. Chem.* **2015**, *80*, 9108–9117. [[CrossRef](#)]
20. Zhang, J.; Quan, Y.; Lin, Z.; Xie, Z. Insight into Reaction Mechanism of [2+2+1] Cross-Cyclootrimerization of Carboryne with Alkene and Trimethylsilylaryllalkyne Mediated by Nickel Complex. *Organometallics* **2014**, *33*, 3556–3563. [[CrossRef](#)]
21. Huo, R.-P.; Guo, L.-H.; Zhang, F.-Q.; Zhang, X. Multiple Electronic State Mechanism for Carboryne Reaction with Benzene: A DFT Study. *Int. J. Quantum Chem.* **2017**, *117*, e25372. [[CrossRef](#)]
22. Mu, W.H.; Ma, Y.; Fang, D.C.; Wang, R.; Zhang, H.N. Computational Insights into the Diels-Alder-like Reactions of 1-Iodo-2-Lithio-*o*-Carborane with Fulvenes. *Acta Chimica Sinica* **2018**, *76*, 55–61. [[CrossRef](#)]
23. Zhao, D.; Zhang, J.; Xie, Z. 1,3-Dehydro-*o*-Carborane: Generation and Reaction with Arenes. *Angew. Chem. Int. Ed.* **2014**, *53*, 8488–8491. [[CrossRef](#)] [[PubMed](#)]
24. Qiu, Z.; Xie, Z. Palladium/Nickel-Cocatalyzed Cycloaddition of 1,3-Dehydro-*o*-Carborane with Alkynes. Facile Synthesis of C,B-Substituted Carboranes. *J. Am. Chem. Soc.* **2010**, *132*, 16085–16093. [[CrossRef](#)] [[PubMed](#)]
25. Quan, Y.; Qiu, Z.; Xie, Z. Transition-Metal-Mediated Three-Component Cascade Cyclization: Selective Cage B-C(sp²) Coupling of Carborane with Aromatics and Synthesis of Carborane-Fused Tricyclics. *J. Am. Chem. Soc.* **2014**, *136*, 7599–7602. [[CrossRef](#)] [[PubMed](#)]

26. Quan, Y.; Zhang, J.; Xie, Z. Three-Component [2+2+1] Cross-Cyclotrimerization of Carboryne, Unactivated Alkene, and Trimethylsilylalkyne Co-Mediated by Zr and Ni. *J. Am. Chem. Soc.* **2013**, *135*, 18742–18745. [[CrossRef](#)] [[PubMed](#)]
27. Mu, W.-H.; Liu, W.-Z.; Cheng, R.-J.; Fang, D.-C. Electronic Effect-Guided, Palladium-Catalyzed Regioselective B-H Activation and Multistep Diarylation of *o*-Carboranes with Aryl Iodides. *ACS Omega* **2019**, *4*, 465–474. [[CrossRef](#)]
28. Frisch, M.J.; Trucks, G.W.; Schlegel, H.B.; Scuseria, G.E.; Robb, M.A.; Cheeseman, J.R.; Scalmani, G.; Barone, V.; Mennucci, B.; Petersson, G.A.; et al. *Gaussian 09, Revision D.01*; Gaussian, Inc.: Wallingford, CT, USA, 2013.
29. Tawada, Y.; Tsuneda, T.; Yanagisawa, S.; Yanai, T.; Hirao, K. A Long-range-corrected Time-dependent Density Functional Theory. *J. Chem. Phys.* **2004**, *120*, 8425–8433. [[CrossRef](#)]
30. Vydrov, O.A.; Scuseria, G.E. Assessment of A Long Range Corrected Hybrid Functional. *J. Chem. Phys.* **2006**, *125*, 234109. [[CrossRef](#)]
31. Yanai, T.; Tew, D.P.; Handy, N.C. A New Hybrid Exchange-correlation Functional Using the Coulomb-attenuating Method (CAM-B3LYP). *Chem. Phys. Lett.* **2004**, *393*, 51–57. [[CrossRef](#)]
32. Lee, C.; Yang, W.; Parr, R.G. Development of the Colle-Salvetti Correlation-Energy Formula into a Functional of the Electron Density. *Phys. Rev. B* **1988**, *37*, 785–789. [[CrossRef](#)] [[PubMed](#)]
33. Becke, A.D. Density-functional Thermochemistry. III. The Role of Exact Exchange. *J. Chem. Phys.* **1993**, *98*, 5648–5652. [[CrossRef](#)]
34. Grimme, S.; Antony, J.; Ehrlich, S.; Krieg, H. A Consistent and Accurate Ab Initio Parametrization of Density Functional Dispersion Correction (DFT-D) for the 94 Elements H-Pu. *J. Chem. Phys.* **2010**, *132*, 154104. [[CrossRef](#)] [[PubMed](#)]
35. Chai, J.-D.; Head-Gordon, M. Long-Range Corrected Hybrid Density Functionals with Damped Atom-Atom Dispersion Corrections. *Phys. Chem. Chem. Phys.* **2008**, *10*, 6615–6620. [[CrossRef](#)] [[PubMed](#)]
36. Godbout, N.; Salahub, D.R.; Andzelm, J.; Wimmer, E. Optimization of Gaussian-type Basis Sets for Local Spin Density Functional Calculations. Part I. Boron Through Neon, Optimization Technique and Validation. *Can. J. Chem.* **1992**, *70*, 560–571. [[CrossRef](#)]
37. Sosa, C.; Andzelm, J.; Elkin, B.C.; Wimmer, E.; Dobbs, K.D.; Dixon, D.A. A Local Density Functional Study of the Structure and Vibrational Frequencies of Molecular Transition-Metal Compounds. *J. Phys. Chem.* **1992**, *96*, 6630–6636. [[CrossRef](#)]
38. Schäfer, A.; Horn, H.; Ahlrichs, R. Fully Optimized Contracted Gaussian-Basis Sets for Atoms Li to Kr. *J. Chem. Phys.* **1992**, *97*, 2571–2577. [[CrossRef](#)]
39. Schäfer, A.; Huber, C.; Ahlrichs, R. Fully Optimized Contracted Gaussian-Basis Sets of Triple zeta Valence Quality for Atoms Li to Kr. *J. Chem. Phys.* **1994**, *100*, 5829–5835. [[CrossRef](#)]
40. Gonzalez, C.; Schlegel, H.B. An Improved Algorithm for Reaction Path Following. *J. Chem. Phys.* **1989**, *90*, 2154–2161. [[CrossRef](#)]
41. Gonzalez, C.; Schlegel, H.B. Reaction Path Following in Mass-Weighted Internal Coordinates. *J. Phys. Chem.* **1990**, *94*, 5523–5527. [[CrossRef](#)]
42. Fukui, K. The Path of Chemical Reactions - the IRC Approach. *Acc. Chem. Res.* **1981**, *14*, 363–368. [[CrossRef](#)]
43. Miertuš, S.; Scrocco, E.; Tomasi, J. Electrostatic Interaction of a Solute with a Continuum. A Direct Utilizaion of AB Initio Molecular Potentials for the Prevision of Solvent Effects. *Chem. Phys.* **1981**, *55*, 117–129. [[CrossRef](#)]
44. York, D.M.; Karplus, M. A Smooth Solvation Potential Based on the Conductor-Like Screening Model. *J. Phys. Chem.* **1999**, *103*, 11060–11079. [[CrossRef](#)]
45. Tao, J.-Y.; Mu, W.-H.; Chass, G.A.; Tang, T.-H.; Fang, D.-C. Balancing the Atomic Waistline: Isodensity-Based SCRF Radii for Main-Group Elements and Transition Metals. *Int. J. Quantum Chem.* **2013**, *113*, 975–984. [[CrossRef](#)]
46. Fang, D.-C. *THERMO Program*; Beijing Normal University: Beijing, China, 2013; This program can generate thermodynamic data in solution under given temperature, based on normally terminated Gaussian jobs with “freq” and “volume” keywords.
47. Reed, A.E.; Curtiss, L.A.; Weinhold, F. Intermolecular Interactions from a Natural Bond Orbital, Donor-Acceptor Viewpoint. *Chem. Rev.* **1988**, *88*, 899–926. [[CrossRef](#)]
48. Reed, A.E.; Weinstock, R.B.; Weinhold, F. Natural Population Analysis. *J. Chem. Phys.* **1985**, *83*, 735–746. [[CrossRef](#)]

49. Carpenter, J.E.; Weinhold, F.J. Analysis of the Geometry of the Hydroxymethyl Radical by the “Different Hybrids for Different Spins” Natural Bond Orbital Procedure. *J. Mol. Struct.-THEOCHEM* **1988**, *169*, 41–62. [[CrossRef](#)]
50. Hostaš, J.; Řezáč, J. Accurate DFT-D3 Calculations in a Small Basis Set. *J. Chem. Theory Comput.* **2017**, *13*, 3575–3585. [[CrossRef](#)]
51. Masson-Makdissi, J.; Vandavasi, J.K.; Newman, S.G. Switchable Selectivity in the Pd-Catalyzed Alkylative Cross-Coupling of Esters. *Org. Lett.* **2018**, *20*, 4094–4098. [[CrossRef](#)]
52. Kim, S.W.; Schwartz, L.A.; Zbieg, J.R.; Stivala, C.E.; Krische, M.J. Regio- and Enantioselective Iridium-Catalyzed Amination of Racemic Branched Alkyl-Substituted Allylic Acetates with Primary and Secondary Aromatic and Heteroaromatic Amines. *J. Am. Chem. Soc.* **2019**, *141*, 671–676. [[CrossRef](#)]
53. Dong, C.-C.; Xiang, J.-F.; Xu, L.-J.; Gong, H.-Y. From CO₂ to 4H-Quinolizin-4-ones: A One-Pot Multicomponent Approach via Ag₂O/Cs₂CO₃ Orthogonal Tandem Catalysis. *J. Org. Chem.* **2018**, *83*, 9561–9567. [[CrossRef](#)] [[PubMed](#)]
54. Koga, Y.; Kaneda, T.; Saito, Y.; Murakami, K.; Itami, K. Synthesis of Partially and Fully Fused Polyaromatics by Annulative Chlorophenylene Dimerization. *Science* **2018**, *359*, 435–439. [[CrossRef](#)]
55. Swyka, R.A.; Zhang, W.; Richardson, J.; Ruble, J.C.; Krische, M.J. Rhodium-Catalyzed Aldehyde Arylation via Formate-Mediated Transfer Hydrogenation: Beyond Metallic Reductants in Grignard/Nozaki-Hiyami-Kishi-Type Addition. *J. Am. Chem. Soc.* **2019**, *141*, 1828–1832. [[CrossRef](#)] [[PubMed](#)]
56. Baker, J.; Scheiner, A.; Andzelm, J. Spin contamination in density functional theory. *Chem. Phys. Lett.* **1993**, *216*, 380–388. [[CrossRef](#)]
57. Quan, Y.; Xie, Z. Palladium-Catalyzed Regioselective Intramolecular Coupling of *o*-Carborane with Aromatics via Direct Cage B-H Activation. *J. Am. Chem. Soc.* **2015**, *137*, 3502–3505. [[CrossRef](#)] [[PubMed](#)]
58. Ding, L.; Ishida, N.; Murakami, M.; Morokuma, K. Sp³-sp² vs. sp³-sp³ C-C Site Selectivity in Rh-Catalyzed Ring Opening of Benzocyclobutenol: A DFT Study. *J. Am. Chem. Soc.* **2014**, *136*, 169–178. [[CrossRef](#)] [[PubMed](#)]
59. Li, Y.; Fang, D.-C. DFT Calculations on Kinetic Data for Some [4+2] Reactions in Solution. *Phys. Chem. Chem. Phys.* **2014**, *16*, 15224–15230. [[CrossRef](#)] [[PubMed](#)]
60. Armstrong, A.; Boto, R.A.; Dingwall, P.; Contreras-Garcia, J.; Harvey, M.J.; Mason, N.J.; Rzepa, H.S. The Houk-List transition States for Organocatalytic Mechanisms Revisited. *Chem. Sci.* **2014**, *5*, 2057–2071. [[CrossRef](#)]
61. Fuentealba, P.; Preuss, H.; Stoll, H.; Szentpály, L.V. A Proper Account of Core-polarization with Pseudopotentials: Single Valence-Electron Alkali Compounds. *Chem. Phys. Lett.* **1982**, *89*, 418–422. [[CrossRef](#)]



© 2019 by the authors. Licensee MDPI, Basel, Switzerland. This article is an open access article distributed under the terms and conditions of the Creative Commons Attribution (CC BY) license (<http://creativecommons.org/licenses/by/4.0/>).